
Long Range Frequency Tuning for QML

Michael Poppel^{1,2} Jonas Stein^{1,2} Sebastian Wölkert² Markus Baumann² Claudia Linnhoff-Popien²

Abstract

Quantum machine learning models using angle encoding naturally represent truncated Fourier series, providing universal function approximation capabilities with sufficient circuit depth. For unary fixed-frequency encodings, circuit depth scales as $\mathcal{O}(\omega_{\max}(\omega_{\max} + \varepsilon^{-2}))$ with target frequency magnitude ω_{\max} and precision ε . Trainable-frequency approaches theoretically reduce this to match the target spectrum size, requiring only as many encoding gates as frequencies in the target spectrum. Despite this compelling efficiency, their practical effectiveness hinges on a key assumption: that gradient-based optimization can drive prefactors to arbitrary target values. We demonstrate through systematic experiments that frequency prefactors exhibit limited trainability: movement is constrained to approximately ± 1 units with typical learning rates. When target frequencies lie outside this reachable range, optimization frequently fails. To overcome this frequency reachability limitation, we propose grid-based initialization using ternary encodings, which generate dense integer frequency spectra. While this approach requires $\mathcal{O}(\log_3 \omega_{\max})$ encoding gates—more than the theoretical optimum but exponentially fewer than fixed-frequency methods—it ensures target frequencies lie within the locally reachable range. On synthetic target functions deliberately constructed with three shifted high frequencies to isolate the reachability challenge, ternary grid initialization achieves a median R^2 score of 0.9969, compared to 0.1841 for the trainable-frequency baseline. For the real-world Flight Passengers dataset, which contains a broader frequency distribution including lower frequencies, ternary grid initialization achieves a median R^2 score of 0.9671 across 10 random ini-

tializations, representing a 22.8% improvement over trainable-frequency initialization (median $R^2 = 0.7876$).

1. Introduction

The identification of latent relationships within complex, high-dimensional datasets represents a fundamental challenge across numerous scientific and commercial domains. Drug development, for example, requires modeling quantum effects such as electron delocalization and chemical bonding, leading to exponential scaling when computed classically (Niazi, 2025). Similarly, financial markets exhibit complex, high-dimensional feature dependencies that traditional modeling approaches struggle to capture, as they typically assume constant correlations and neglect tail dependencies (Kolawole, 2024). Both domains exemplify problems where the dimensionality and complexity of relationships exceed the practical capabilities of classical approaches. Quantum machine learning (QML) emerges as a promising paradigm to address these challenges, offering theoretical advantages over classical approaches. Studies demonstrate that quantum models can represent more complex functions than classical counterparts (Mitarai et al., 2018), exhibiting higher effective dimensionality and potential computational advantages compared to traditional neural networks (Abbas et al., 2021). However, substantial challenges remain for QML. Barren plateaus limit the number of trainable qubits (Ragone et al., 2024), while NISQ hardware constraints hinder practical deployment. Although qubit counts continue rising and error rates are improving, circuit depth must remain shallow to mitigate noise accumulation, making efficient parameter utilization critical. Analogous to activation functions in classical neural networks, quantum circuits achieve expressivity through angle encoding, data re-uploading, and entangling gates. As shown by Schuld et al. (2021), these mechanisms enable quantum models to represent truncated Fourier series. Recent research has focused on identifying resource-efficient circuit structures, with Pérez-Salinas et al. (2025) and Yu et al. (2024) establishing minimal architectures for fixed-frequency encodings. Trainable-frequency (TF) quantum models extend this paradigm by learning the generators for data encoding unitaries, enabling non-regularly spaced fre-

¹Aqarios GmbH, Munich, Bavaria, Germany

²Department of Computer Science, LMU Munich, Munich, Bavaria, Germany. Correspondence to: Michael Poppel <michael.poppel@aqarios.com>.

quencies and flexible spectral richness tailored to specific tasks (Jaderberg et al., 2024). Theoretically, TF models can reduce encoding gate requirements from polynomial scaling in fixed-frequency models to matching the target spectrum size itself, assuming gradient-based optimization can drive prefactors to arbitrary target values. However, we demonstrate that this assumption fails in practice. By shifting the target frequency spectrum by 10 units relative to the original example from Jaderberg et al. (2024), we reveal that TF models struggle to reach frequencies beyond a narrow range around initialization, with reliable convergence occurring only for nearby target frequencies. To address this limitation, we propose a grid-based initialization strategy using ternary encoding gates (Peters & Schuld, 2023; Kordzanganeh et al., 2023; Shin et al., 2023) that places frequencies at regular, densely spaced intervals across the target spectrum, enabling the model to achieve the desired frequency representation through local fine-tuning during training.

We summarize our contributions as follows:

- We demonstrate that TF quantum models exhibit limited frequency reachability, with reliable convergence occurring only when target frequencies lie within a narrow range around initialization values.
- We systematically analyze and formalize parameter scaling requirements across trainable-frequency models and fixed-frequency approaches, showing that ternary encodings can also be used to achieve exponential reduction in encoding gates while maintaining identical ansatz parameter requirements.
- We introduce a grid-based initialization strategy using ternary encoding gates that establishes a dense frequency spectrum with $|\Omega| = 3^k$ frequencies for k encoding gates, ensuring target frequencies lie within the locally reachable optimization range and achieving reliable convergence where standard trainable-frequency approaches fail.

2. Theoretical Background

2.1. Fixed-Frequency Variational Quantum Circuits

Variational quantum circuits (VQCs) represent a prominent class of QML models that encode and process data through parametrized quantum operations.

Definition 2.1 (Unary Fixed-Frequency VQC). An L -layer unary fixed-frequency VQC with angle encoding consists of feature maps (FM) $S(x) = e^{ixH}$ where $H = \frac{1}{2}\sigma$ for a Pauli operator $\sigma \in \{\sigma_x, \sigma_y, \sigma_z\}$ implementing rotation gates $R(x) = e^{-i\frac{x}{2}\sigma}$ with $R \in \{R_x, R_y, R_z\}$ and unit prefactors, parametrized ansatz layers $W_i(\theta_i)$ with trainable parameters $\theta = (\theta_0, \dots, \theta_L)$, and an observable M

for measurement. The circuit is formed by interleaving feature maps and ansatz layers:

$$U(x, \theta) = W_L(\theta_L)S(x) \cdots S(x)W_0(\theta_0), \quad (1)$$

with model output

$$f_\theta(x) = \langle 0|U^\dagger(x, \theta)MU(x, \theta)|0\rangle. \quad (2)$$

Parameters are optimized by minimizing a loss function $\mathcal{L}(\theta)$: $\theta^* = \underset{\theta}{\operatorname{argmin}} \mathcal{L}(\theta)$ (Farhi & Neven, 2018).

Fourier Representation. A fundamental property of angle-encoded quantum circuits is their representation as truncated Fourier series.

Theorem 2.2 (Fourier Representation of VQCs (Schuld et al., 2021)). *For a variational quantum circuit with angle encoding, the model output $f_\theta(x)$ can be expressed as a Fourier series:*

$$f_\theta(x) = \sum_{\omega \in \Omega} c_\omega(\theta)e^{i\omega x}, \quad (3)$$

where Ω is the frequency spectrum determined by the feature map $S(x)$ and observable M , and $c_\omega(\theta) \in \mathbb{C}$ are parameter-dependent Fourier coefficients. For unary fixed-frequency circuits with L layers, $|\Omega| = 2L + 1$.

This representation extends to all angle-encoding architectures, including the ternary fixed-frequency and trainable-frequency circuits introduced below, though with different frequency spectra determined by their respective prefactor configurations. The frequency spectrum can be generated through equivalent circuit architectures: *serial* (L FMs applied sequentially to the same qubit), *parallel* (L FMs applied simultaneously to L distinct qubits), or *hybrid* (l_s serial and l_p parallel FMs with $l_s \cdot l_p = L$), all generating identical spectra (Holzer & Turkalj, 2024).

Corollary 2.3 (Parameter Scaling (Schuld et al., 2021)). *For an L -layer angle-encoding circuit with frequency spectrum $|\Omega| = 2L + 1$, independent control of all Fourier coefficients requires at least $M \geq 2L + 1$ ansatz parameters.*

These parameters must be independently trainable to provide actual degrees of freedom for coefficient control. Parameter sharing or architectural constraints that reduce the effective number of independent parameters will limit expressivity accordingly.

Definition 2.4 (Ternary Fixed-Frequency VQC). A ternary fixed-frequency variational quantum circuit extends Definition 2.1 by using exponentially-spaced prefactors in the FMs. The FM in layer i takes the form $S_i(x) = e^{i3^i xH}$ where the prefactor 3^i is fixed for $i \in \{0, \dots, L - 1\}$. The circuit structure and output follow Definition 2.1, with these ternary FMs interleaved with ansatz layers.

This encoding strategy generates a dense integer frequency spectrum, achieving exponential growth in the number of unique frequencies with each additional encoding gate. Notably, ternary encodings achieve the largest possible cardinality for separable encoding generators (Peters & Schuld, 2023).

2.2. Trainable-Frequency Variational Quantum Circuits

The circuits discussed above use fixed prefactors in the FMs, limiting the frequency spectrum to predetermined values. We now introduce trainable-frequency circuits where these prefactors become optimizable parameters.

Definition 2.5 (Unary Trainable-Frequency VQC). A unary trainable-frequency variational quantum circuit extends Definition 2.1 by parameterizing the FM prefactors. The FM takes the form $S(x, \alpha) = e^{i\alpha x H}$ where the prefactor $\alpha \in \mathbb{R}^L$ is trainable alongside the ansatz parameters θ . For angle encoding with Pauli operators, this yields rotation gates $R(x, \alpha) = e^{-i\frac{\alpha x}{2}\sigma}$ where $R \in \{R_x, R_y, R_z\}$. The circuit becomes

$$U(x, \theta, \alpha) = W_L(\theta_L)S(x, \alpha_L) \cdots S(x, \alpha_1)W_0(\theta_0), \quad (4)$$

with model output

$$f_{\theta, \alpha}(x) = \langle 0|U^\dagger(x, \theta, \alpha)MU(x, \theta, \alpha)|0\rangle. \quad (5)$$

2.3. Quantum Models as Universal Function Approximators

Having established that angle-encoded quantum circuits represent truncated Fourier series, we now examine their universal approximation capabilities and compare the parameter requirements across different architectural choices.

Theorem 2.6 (Universal Approximation for Trainable-Frequency VQCs (Yu et al., 2022; Pérez-Salinas et al., 2021)). *Consider a unary trainable-frequency circuit as defined in Definition 2.5 where the ansatz layers $W(\theta)$ form a universal gate set. For any continuous function $f : [0, 1]^d \rightarrow [-1, 1]$ and $\varepsilon > 0$, there exists circuit depth L and parameters θ, α such that*

$$|f_{\theta, \alpha}(x) - f(x)| < \varepsilon \quad \forall x \in [0, 1]^d. \quad (6)$$

Importantly, Yu et al. (2022) demonstrate that the choice of Pauli rotation gate for encoding does not affect approximation capability, provided the ansatz gates are universal.

3. Comparison of Encoding Gate and Ansatz Parameter Requirements

Theorem 2.6 establishes that for any target function f and precision $\varepsilon > 0$, there exists a circuit depth sufficient for

unary trainable-frequency circuits to achieve approximation.

Assumption 3.1. We denote by k_{opt} the minimum circuit depth (number of encoding gates) required for unary trainable-frequency circuits to achieve approximation error below a specified ε for a given target function. We use k_{opt} as the baseline for comparing different architectural choices.

Remark 3.2 (Dynamic Frequency Spectrum). Unlike fixed-frequency circuits, the frequency spectrum $|\Omega|$ in trainable-frequency circuits depends on the evolved prefactor values $\{\alpha_i\}$. For k_{opt} encoding gates with prefactors initialized at unity, the initial spectrum contains $|\Omega| = 2k_{\text{opt}} + 1$ frequencies. However, during training:

- Minimum spectrum: If all prefactors converge to zero, $|\Omega| = 1$ (zero frequency only, i.e., constant output)
- Maximum spectrum: If prefactors become distinct powers of 3, $|\Omega| = 3^{k_{\text{opt}}}$ frequencies

By Corollary 2.3, since the spectrum can grow to $|\Omega| = 3^{k_{\text{opt}}}$ during training, a conservative design requires $|\theta| \geq 3^{k_{\text{opt}}}$ ansatz parameters to maintain full expressivity.

Proposition 3.3 (Unary Fixed-Frequency Requirements (Pérez-Salinas et al., 2025)). *Approximating a single trainable-frequency gate with prefactor $|\alpha_i| \leq k_{\text{opt}}$ using unary fixed-frequency gates with unit prefactors requires $\mathcal{O}(|\alpha_i| + \varepsilon^{-2})$ encoding gates to achieve approximation error ε . Consequently, approximating a complete trainable-frequency circuit with k_{opt} trainable encoding gates requires*

$$k \in \mathcal{O}(k_{\text{opt}} \cdot (k_{\text{opt}} + \varepsilon^{-2})) \quad (7)$$

unary fixed-frequency encoding gates. These gates generate a fixed frequency spectrum with $|\Omega| = 2k + 1$ frequencies. By Corollary 2.3, the ansatz requires $|\theta| = 2k + 1$ parameters.

Proof. Each trainable frequency can be approximated by a truncated Fourier series, requiring circuit depth proportional to both the frequency magnitude and the inverse precision squared (Pérez-Salinas et al., 2025). Summing over all k_{opt} trainable gates yields the encoding gate complexity. The ansatz parameter requirement follows from Corollary 2.3, which establishes that $|\Omega| = 2k + 1$ frequencies require at least $2k + 1$ trainable parameters for arbitrary coefficient control. \square

Unlike trainable-frequency circuits where the spectrum can evolve during training (Remark 3.2), fixed-frequency circuits have a constant frequency spectrum determined at initialization, and thus require a fixed number of ansatz parameters throughout training.

Proposition 3.4 (Ternary Fixed-Frequency Requirements). *Approximating a single trainable-frequency gate with prefactor $|\alpha_i| \leq k_{opt}$ using ternary fixed-frequency gates with prefactors $\{3^0, 3^1, \dots\}$ requires $\mathcal{O}(\log_3 |\alpha_i| + \log_3(\varepsilon^{-1}))$ encoding gates to achieve approximation error ε . Consequently, approximating a complete trainable-frequency circuit with k_{opt} trainable encoding gates requires*

$$k \in \mathcal{O}(k_{opt} \cdot (\log_3 k_{opt} + \log_3(\varepsilon^{-1}))) \quad (8)$$

ternary fixed-frequency encoding gates. Despite the exponential reduction in encoding gates, these gates generate the same frequency spectrum size as the unary fixed approach, $|\Omega| = 2k_{unary} + 1$, where $k_{unary} \in \mathcal{O}(k_{opt}^2 + k_{opt}\varepsilon^{-2})$ from Proposition 3.3. By Corollary 2.3, the ansatz requires $|\theta| = 2k_{unary} + 1$ parameters.

Proof. The proof follows by adjusting Corollary 2 in Pérez-Salinas et al. (2025) to account for ternary encoding efficiency. A complete derivation is provided in Section A. \square

The key advantage of ternary encodings is the exponential reduction in encoding gate count while maintaining identical ansatz parameter requirements, as both architectures generate frequency spectra of the same cardinality.

Remark 3.5 (Parameter Generation Capacity). In unary fixed-frequency architectures, a sufficient number of independently trainable parameters can be generated on a single qubit, as each additional layer introduces new frequencies and corresponding parameters. In contrast, ternary encoding induces exponential growth in the number of accessible frequencies, which cannot be accommodated by simply increasing circuit depth. The number of independently controllable parameters per ansatz layer is upper bounded by $\max(\dim(\mathfrak{g})) = 4^q - 1$ for a q -qubit system, where \mathfrak{g} denotes the dynamical Lie algebra (DLA) generated by the circuit (Larocca et al., 2024). Consequently, ternary encoding schemes with k encoding gates generating $|\Omega| = 3^k$ frequencies must balance this exponential growth with a corresponding increase in circuit width: $q \geq \log_4(3^k + 1)$ qubits are required for single-layer ansatz architectures to provide sufficient parameterization.

Table 1 summarizes the key scaling differences. Ternary fixed-frequency encodings achieve exponential improvement in encoding gate count compared to unary fixed approaches, while both fixed-frequency methods share identical ansatz parameter requirements that remain constant during training. Trainable-frequency circuits offer the most efficient encoding gate usage but have a dynamic frequency spectrum (Remark 3.2), requiring careful provisioning of ansatz parameters. The unary trainable-frequency approach presents a compelling option due to its substantial parameter efficiency: requiring only k_{opt} encoding gates,

compared to the quadratic scaling of fixed-frequency methods. When the number of frequencies in the target function is known a priori, this approach becomes particularly attractive—as demonstrated by Jaderberg et al. (2024), who achieve near-perfect approximation of a three-frequency target function using exactly three trainable encoding gates, matching the theoretical optimum.

4. Frequency Reachability Limitations in Trainable Models

Despite the compelling efficiency of trainable-frequency approaches established in the previous section, their practical effectiveness hinges on a key assumption: that gradient-based optimization can drive prefactors to arbitrary target values. To test this assumption, we systematically examine the frequency reachability of trainable-frequency models by measuring how far prefactors can move from initialization during training.

4.1. Experimental Setup

Reachability validation. We reproduce the trainable-frequency experiment from Jaderberg et al. (2024), which successfully fitted a target function with frequency spectrum $\Omega_1 = \{1, 1.2, 3\}$ using trainable unary prefactors initialized to 1.0. To test frequency reachability, we shift the entire target frequency spectrum by 10 units to $\Omega_2 = \{11, 11.2, 13\}$, testing whether trainable prefactors can reach frequencies far from their initialization. We analyze prefactor evolution and gradient behavior on this shifted spectrum to understand the optimization dynamics underlying the reachability limitation.

The target functions are defined as truncated Fourier series:

$$t(x) = c_0 + \sum_{i=1}^3 [a_i \cos(\omega_i x) + b_i \sin(\omega_i x)] \quad (9)$$

where $\omega_i \in \Omega$ represents the target frequency set, and coefficients c_0, a_i, b_i are randomly sampled from $[0, 1)$. For all experiments, we generate 10 distinct target functions per frequency configuration (each with randomly sampled coefficients) and train each target with 10 different weight initializations, yielding 100 runs per configuration.

Robustness evaluation. To systematically evaluate how ternary grid initialization performs across varying frequency ranges, we conduct additional experiments with randomly shifted spectra. Starting from the original spectrum $\Omega_1 = \{1, 1.2, 3\}$ from Jaderberg et al. (2024), we add random offsets drawn from $\mathcal{N}(\mu, 1)$ with mean μ ranging from 0 to 9. This deliberately shifts all frequencies toward higher values for illustrative purposes—isolating the reachability challenge—whereas real-world datasets typically contain broader frequency distributions that retain

Table 1. Comparison of parameter scaling for different VQC architectures relative to the trainable-frequency baseline k_{opt} from Assumption 3.1.

Architecture	Encoding Gates	Ansatz Parameters	Spectrum
Unary Trainable	k_{opt}	$2k_{\text{opt}} + 1$ (initial) $\Omega(3^{k_{\text{opt}}})$ (worst-case)	Dynamic
Unary Fixed	$\mathcal{O}(k_{\text{opt}}(k_{\text{opt}} + \varepsilon^{-2}))$	$\mathcal{O}(k_{\text{opt}}^2 + k_{\text{opt}}\varepsilon^{-2})$	Fixed
Ternary Fixed	$\mathcal{O}(k_{\text{opt}}(\log_3 k_{\text{opt}} + \log_3(\varepsilon^{-1})))$	$\mathcal{O}(k_{\text{opt}}^2 + k_{\text{opt}}\varepsilon^{-2})$	Fixed

lower-frequency components alongside higher frequencies.

Model validation uses an 80/20 random train/test split for all datasets. All experiments for the synthetic target functions use identical quantum circuit architectures with 3 qubits and 3 FMs; for the real-world Flight Passengers dataset (Box & Jenkins, 1976) we use 4 qubits and 4 FMs. The ansatz blocks employ PennyLane’s special unitary gates ($qml.SpecialUnitary(\theta)$), providing 63 parameters per layer for the 3-qubit circuits and 255 parameters per layer for the 4-qubit architecture and ensuring the full dimension of the DLA is reached. This guarantees sufficient expressivity to avoid spurious local minima caused by insufficient parameter counts (Larocca et al., 2024).¹ The classical baseline uses a feedforward architecture with two hidden layers of 64 units each, ReLU activations, and 10% dropout, trained with Adam (learning rate 0.001) for 500 epochs. Further details for the experimental set-up can be found in Section D.

4.2. Results

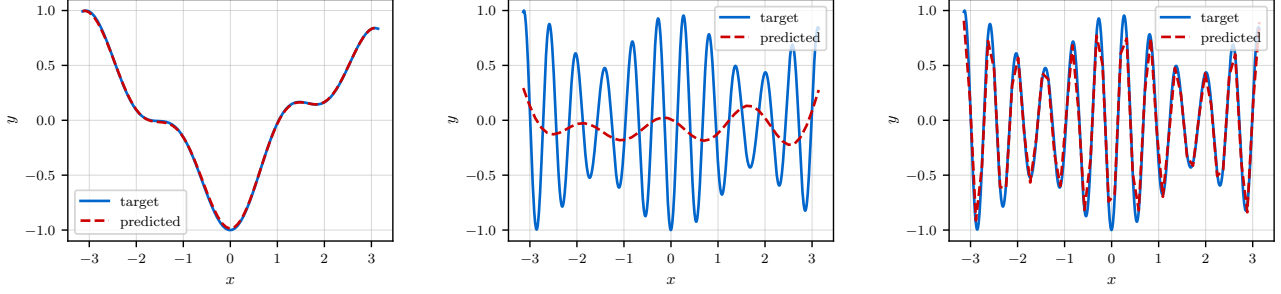
Figure 1 demonstrates limitations in frequency reachability. While the original experiment with Ω_1 converges successfully to the target function (Figure 1a), our frequency-shifted variant with Ω_2 fails to achieve adequate fits when using the same unary initialization strategy (Figure 1b). Despite identical optimization procedures and sufficient training time, the model remains constrained to a limited range around its initialization. To systematically quantify prefactor mobility, we must address a technical challenge: when all three prefactors are initialized to the identical value of 1.0, the optimizer sometimes fails to distinguish between them during early training iterations, causing them to update in lock-step rather than independently. This behavior is shown in Figure 5, where prefactors occasionally remain identical for extended periods before diverging. To ensure independent prefactor evolution from the start, we introduce slightly perturbed initial values of $\{1.01, 1.02, 1.03\}$ for our detailed analysis. This small per-

¹While full special unitary parametrization becomes impractical for larger qubit counts due to exponential parameter scaling, overlapping 2-qubit special unitary gates provide a scalable alternative with strong empirical performance (Wierichs et al., 2025).

turbation has only marginal effect on the final R^2 scores (see Figure 6) but ensures that gradient signals are distinct for each prefactor from the first optimization step. With this initialization, Figure 2a reveals that prefactors exhibit severely limited mobility during optimization. For learning rates of 0.001 and 0.01, both mean and maximum displacement remain below 1—far too small to reach the target frequency range of 11–13. Even with an aggressive learning rate of 0.1, the maximum displacement reaches only approximately 7, and the mean displacement remains around 2, indicating that most prefactors fail to achieve the required displacement.

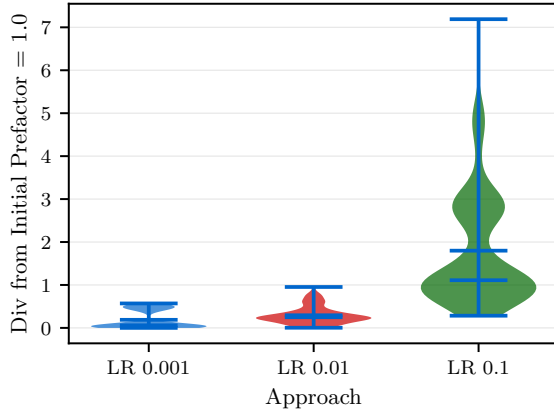
4.3. Analysis

The gradient analysis in Figure 2b reveals the underlying cause of this reachability limitation. We compute prefactor gradients for a target function with spectrum $\Omega_2 = \{11, 11.2, 13\}$ after the first optimizer iteration for various initial prefactor values, effectively sweeping across the parameter space. The results show that gradient magnitudes are significantly stronger when initial prefactors lie near the target frequencies. Conversely, prefactors initialized far from targets receive weak gradient signals, providing insufficient directional information for the optimizer. This creates a fundamental challenge: the optimization landscape exhibits strong locality, with effective gradient information available only within a limited neighborhood of each target frequency. When prefactors are initialized outside this neighborhood, the loss surface provides inadequate guidance for convergence, resulting in the limited mobility observed in Figure 2a. The prefactor evolution during training further illustrates this local fine-tuning behavior. Figure 3 shows that with learning rates of 0.001 and 0.01, unary prefactors remain confined near their initial values. Only the aggressive learning rate of 0.1 enables occasional long-distance movement for unary prefactors. However, this produces unreliable and inconsistent results, as evidenced by the low density of large deviations in the violin plot (Figure 2a). These observations reveal a critical gap between theoretical flexibility and practical trainability in trainable-frequency models. While such models can theoretically represent arbitrary frequency

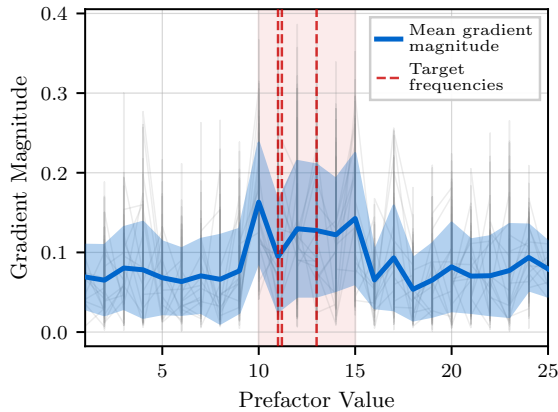


(a) Frequencies from Jaderberg et al. (2024) $\Omega_1 = \{1, 1.2, 3\}$ with unary prefactors. (b) Frequencies $\Omega_2 = \{11, 11.2, 13\}$ with unary prefactors. (c) Frequencies $\Omega_2 = \{11, 11.2, 13\}$ with ternary prefactors.

Figure 1. Target and trained predictions for the original Jaderberg experiment with unary initial prefactors (a), the frequency-shifted variant with unary prefactors showing poor fit (b), and the same shifted frequencies with ternary grid initialization demonstrating successful recovery (c).



(a) Distribution of prefactor displacement from initial values after 5,000 iterations, showing means, medians, and extrema.



(b) Prefactor gradients after the first optimizer iteration for different initial prefactors.

Figure 2. Prefactor displacement and gradient analysis across 100 target functions. Initial prefactors were set to $\{1.01, 1.02, 1.03\}$ to ensure distinct gradient signals from the start of training.

spectra, gradient-based optimization constrains accessible frequencies to a narrow neighborhood around initialization—approximately ± 1 unit for standard learning rates of 0.01 and 0.001. This motivates an alternative approach: rather than relying on long-distance prefactor tuning, we initialize with a dense grid of frequencies that ensures all target frequencies lie within the locally reachable range, as presented in the following section.

5. Dense Grid Initialization via Ternary Trainable-Frequency VQCs

To overcome the frequency reachability limitations demonstrated in Section 4, we propose combining ternary encoding with trainable prefactors.

Definition 5.1 (Ternary Trainable-Frequency VQC). A ternary trainable-frequency VQC extends the unary trainable-frequency architecture (Definition 2.5) by initializing prefactors with exponentially-spaced values $\{\alpha_j^{(0)} = 3^j\}_{j=0}^{k-1}$, which then become trainable during optimization. The circuit structure and output follow Definition 2.5.

For k encoding gates, this initialization generates a dense integer frequency spectrum:

$$\Omega_{\text{grid}}^{(0)} = \left\{ -\left\lfloor \frac{3^k}{2} \right\rfloor, \dots, -1, 0, 1, \dots, \left\lfloor \frac{3^k}{2} \right\rfloor \right\}. \quad (10)$$

Proposition 5.2 (Ternary Trainable-Frequency Requirements). For a ternary trainable-frequency circuit covering target frequencies up to ω_{\max} , the circuit requires $k = \lceil \log_3(2\omega_{\max} + 1) \rceil$ encoding gates and $|\theta| \geq 2\omega_{\max} + 1$ ansatz parameters.

Proof. For k ternary encoding gates, the maximum frequency is $\left\lfloor \frac{3^k}{2} \right\rfloor = \frac{3^k - 1}{2}$. To cover $[-\omega_{\max}, \omega_{\max}]$, we require $\frac{3^k - 1}{2} \geq \omega_{\max}$, yielding $k \geq \log_3(2\omega_{\max} + 1)$. Tak-

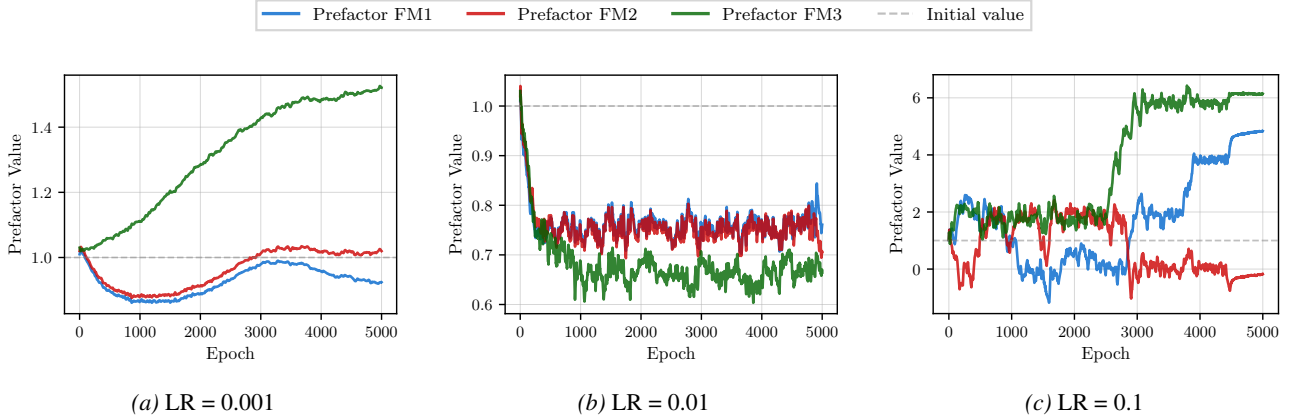


Figure 3. Prefactor evolution for different learning rates with initial prefactors of $\{1.01, 1.02, 1.03\}$ for unary initialization on target functions with frequency spectrum $\Omega_2 = \{11, 11.2, 13\}$. Each panel shows the best-performing run (highest R^2 score) for that learning rate. Only the aggressive learning rate of 0.1 enables substantial prefactor movement, but this occurs unreliably as demonstrated by Figure 6.

ing the ceiling ensures k is a natural number. The ansatz parameter requirement follows from Corollary 2.3. \square

Corollary 5.3 (Ternary Encoding Gate Complexity). *Ternary encoding circuits can approximate arbitrary frequency encodings $e^{i\omega_{\max}xH}$ to precision ϵ using*

$$k \in \mathcal{O}\left(\log_3 \omega_{\max} + \log_3\left(\frac{1}{\epsilon}\right)\right) \quad (11)$$

fixed encoding gates with exponentially-spaced prefactors $\{3^0, 3^1, \dots, 3^{k-1}\}$. This represents an exponential improvement over unary encoding, which requires $\mathcal{O}(\omega_{\max} + \epsilon^{-2})$ encoding gates.

Proof. By Fejér’s theorem and properties of Cesàro means, arbitrary target frequencies can be approximated using truncated Fourier series with coefficients from the ternary frequency spectrum. The logarithmic dependence on both ω_{\max} and ϵ^{-1} follows from the exponential density of ternary encodings. A complete derivation is provided in Section A. \square

Crucially, the dense initial grid ensures all target frequencies within $[-\omega_{\max}, \omega_{\max}]$ lie within $\pm 1/2$ unit of a grid frequency, placing them within the locally reachable optimization range established in Section 4. This architecture represents a practical middle ground between theoretical optimality and reliable convergence. We distinguish two cases relative to the unary trainable-frequency baseline (k_{opt} gates from Assumption 3.1):

Case 1: Sparse target spectra. When the number of target frequencies is small relative to ω_{\max} (i.e., $k_{\text{opt}} \ll \log_3(2\omega_{\max} + 1)$), the unary trainable approach is theoretically more efficient, requiring only k_{opt} encoding gates

and $2k_{\text{opt}} + 1$ ansatz parameters. The ternary grid requires $\lceil \log_3(2\omega_{\max} + 1) \rceil$ gates and $2\omega_{\max} + 1$ parameters—substantially more than the theoretical minimum. However, as demonstrated in Section 4, unary initialization fails to achieve reliable convergence when target frequencies lie beyond a narrow range around initialization, making theoretical efficiency irrelevant in practice.

Case 2: Dense or unknown frequency coverage. When target frequencies span the full range $[-\omega_{\max}, \omega_{\max}]$, unary approaches require $k_{\text{opt}} \approx \omega_{\max}$ encoding gates and $2\omega_{\max} + 1$ ansatz parameters. The ternary grid achieves exponential improvement with only $\mathcal{O}(\log_3 \omega_{\max})$ encoding gates while maintaining identical ansatz parameter requirements. Moreover, when the target spectrum is unknown a priori, ternary initialization provides robust coverage without requiring advance knowledge of specific target frequencies.

The key insight is that ternary grid initialization trades modest parameter overhead in sparse cases for robust reachability, enabling reliable convergence where theoretical optimality alone proves insufficient.

5.1. Experimental Validation

We validate this approach using ternary prefactors $\{1, 3, 9\}$ on the frequency-shifted targets from Section 4, comparing against unary fixed-frequency, ternary fixed-frequency (Definition 2.4), and unary trainable-frequency baselines. The ternary grid $\Omega_{\text{grid}} = \{-13, \dots, 13\}$ encompasses target frequencies $\Omega_2 = \{11, 11.2, 13\}$, enabling accurate fitting (Figure 1c). Testing on frequency-shifted variants (original frequencies $\Omega = \{1, 1.2, 3\}$ plus random offsets from $\mathcal{N}(\mu, 1)$, $\mu \in [0, 9]$), Figure 4 shows trainable ternary prefactors achieve $R^2 > 0.95$ consistently across all 100

runs per shift, while trainable unary prefactors deteriorate with increasing shifts, even underperforming fixed ternary baselines.

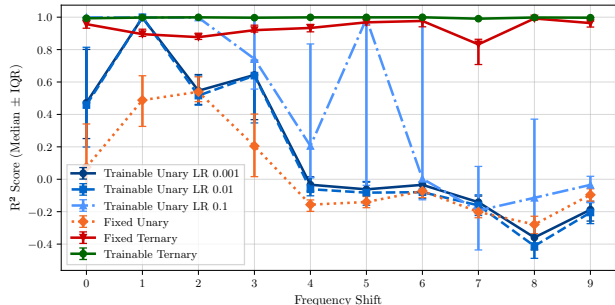


Figure 4. R^2 score interquartile ranges for frequency-shifted targets. Trainable ternary prefactors (LR = 0.001) achieve consistently high scores across all shifts, fixed ternary prefactors come close, while trainable unary and fixed unary prefactors fail.

On the Flight Passengers dataset, ternary trainable-frequency (4-qubit parallel, 510 parameters) achieved median $R^2 = 0.9671$ across 10 runs, exceeding fixed ternary (0.9056), trainable unary (0.7876) and fixed unary (0.7066) (see Figure 7 in Appendix). The smaller performance gap compared to synthetic experiments reflects the dataset’s broader frequency distribution: real-world time series data typically contains lower-frequency components that remain within the reachable range even with unary initialization. For comparison, a classical feedforward network (4,417 parameters) achieved median $R^2 = 0.9828$, demonstrating that ternary trainable-frequency approaches classical performance.

6. Discussion

Understanding the reachability limitation. Our gradient analysis (Section 4) reveals that prefactor gradients vanish rapidly with distance from target frequencies, creating a fundamentally local optimization landscape. This suggests the limitation is not an artifact of our specific optimizer but rather a structural property of the loss surface. One possible explanation is non-stationarity: updating frequency prefactors reshapes the entire loss landscape, potentially invalidating gradient directions for ansatz parameters. The extent of prefactor movement varies with learning rate: The ternary grid with unit spacing accommodates even conservative learning rates for local fine-tuning between adjacent grid points. Preliminary explorations of alternating optimization schemes and adaptive learning rates did not yield systematic improvements, supporting the interpretation that this is a fundamental barrier to long-distance prefactor tuning rather than an optimizer-specific phenomenon.

Practical considerations. While our approach requires specifying a maximum target frequency ω_{\max} , this can be

determined empirically by progressively adding ternary encoding gates until performance converges. Due to logarithmic scaling, this search requires only $\mathcal{O}(\log \omega_{\max})$ iterations. The total parameter requirement of $\mathcal{O}(\omega_{\max})$ ansatz parameters remains necessary across all approaches to independently control frequencies in the target range.

Limitations and caveats. Trainable-frequency models incorporate parameterized classical data processing through learnable prefactors that multiply input data (αx) before quantum encoding. This creates ambiguity regarding whether expressivity originates from classical or quantum components (Yu et al., 2024). Caution is therefore warranted when claiming quantum advantages for such models. Additionally, all approaches discussed here face the *curse of dimensionality* when scaling to higher-dimensional inputs, with parameter requirements scaling as $\mathcal{O}(\exp(d))$ for d -dimensional data (Pérez-Salinas et al., 2025). Current quantum simulators and near-term hardware impose practical limits to moderate-dimensional problems, and whether future fault-tolerant devices can leverage this exponential structure more efficiently than classical approaches remains an open question.

7. Conclusion

We have demonstrated that trainable-frequency quantum models, despite their theoretical promise of minimal gate requirements, face significant practical limitations due to constrained frequency reachability during gradient-based optimization. Through systematic experiments, we quantified this limitation: while prefactor movement ranges from approximately $\pm 1/2$ units with conservative learning rates to ± 7 units with aggressive rates, reliable convergence occurs only within a narrow range around initialization. This causes optimization failure when target frequencies lie outside the locally reachable range. Our proposed ternary grid initialization strategy addresses this limitation by establishing a dense integer frequency spectrum that ensures target frequencies lie within the reachable range from initialization. On synthetic target functions designed to isolate the reachability challenge, this approach achieved median $R^2 = 0.9969$ compared to 0.1841 for standard trainable-frequency initialization. On the real-world Flight Passengers dataset, ternary grid initialization achieved a 22.8% improvement (median $R^2 = 0.9671$ vs 0.7876). By combining the gate efficiency of ternary encodings with trainable prefactors, our approach provides a practical path forward for deploying frequency-adaptive quantum models on near-term hardware, achieving exponential gate reduction while ensuring reliable convergence where theoretical optimality alone proves insufficient.

Acknowledgements

A project partially underlying this report was funded by the German Federal Ministry of Research, Technology and Space under the funding code 01MQ22008A. The sole responsibility for the report’s contents lies with the authors.

Impact Statement

This paper presents work whose goal is to advance the field of (Quantum) Machine Learning. There are many potential societal consequences of our work, none which we feel must be specifically highlighted here.

LLM Statement

Large language models have been used for the production of this paper to polish writing, debug the code for conducting the experiments and generate the code for plotting the results.

Reproducibility Statement

The circuit diagram for the various experiments can be found in Section E. The target functions and a high level description of the experimental set up is provided in Section 4.1 and in more detail in Section D. In the supplementary materials we have included a zip file with the Jupyter notebook for generating the results for the ternary-trainable model shown in Figure 4, together with the dataset and the code for generating the plot with the results.

References

Abbas, A., Sutter, D., Zoufal, C., Lucchi, A., Figalli, A., and Woerner, S. The power of quantum neural networks. *Nature Computational Science*, 1(6): 403–409, June 2021. ISSN 2662-8457. doi: 10.1038/s43588-021-00084-1. URL <http://dx.doi.org/10.1038/s43588-021-00084-1>.

Bergholm, V., Izaac, J., Schuld, M., Gogolin, C., Ahmed, S., Ajith, V., Alam, M. S., Alonso-Linaje, G., Akash-Narayanan, B., Asadi, A., Arrazola, J. M., Azad, U., Banning, S., Blank, C., Bromley, T. R., Cordier, B. A., Ceroni, J., Delgado, A., Matteo, O. D., Dusko, A., Garg, T., Guala, D., Hayes, A., Hill, R., Ijaz, A., Isacsson, T., Ittah, D., Jahangiri, S., Jain, P., Jiang, E., Khandelwal, A., Kottmann, K., Lang, R. A., Lee, C., Loke, T., Lowe, A., McKiernan, K., Meyer, J. J., Montañez-Barrera, J. A., Moyard, R., Niu, Z., O’Riordan, L. J., Oud, S., Panigrahi, A., Park, C.-Y., Polatajko, D., Quesada, N., Roberts, C., Sá, N., Schoch, I., Shi, B., Shu, S., Sim, S., Singh, A., Strandberg, I., Soni, J., Száva, A., Thabet, S., Vargas-Hernández, R. A., Vincent, T., Vitucci, N.,

Weber, M., Wierichs, D., Wiersema, R., Willmann, M., Wong, V., Zhang, S., and Killoran, N. PennyLane: Automatic differentiation of hybrid quantum-classical computations, 2022. URL <https://arxiv.org/abs/1811.04968>.

Box, G. E. P. and Jenkins, G. M. *Time Series Analysis: Forecasting and Control*. Holden-Day, San Francisco, 1976. Dataset: International airline passengers, monthly totals (1949-1960).

DeepMind. Optax: Gradient processing and optimization library in jax. <https://optax.readthedocs.io/en/latest/api/optimizers.html>, 2020. Accessed: 2025-07-29.

Farhi, E. and Neven, H. Classification with quantum neural networks on near term processors, 2018. URL <https://arxiv.org/abs/1802.06002>.

Frostig, R., Johnson, M., and Leary, C. Compiling machine learning programs via high-level tracing. 2018. URL <https://mlsys.org/Conferences/doc/2018/146.pdf>.

Holzer, P. and Turkalj, I. Spectral invariance and maximality properties of the frequency spectrum of quantum neural networks, 2024. URL <https://arxiv.org/abs/2402.14515>.

Jaderberg, B., Gentile, A. A., Berrada, Y. A., Shishenina, E., and Elfving, V. E. Let quantum neural networks choose their own frequencies. *Physical Review A*, 109(4), April 2024. ISSN 2469-9934. doi: 10.1103/physreva.109.042421. URL <http://dx.doi.org/10.1103/PhysRevA.109.042421>.

Kolawole, W. Hybrid financial models for capturing asset correlation structures. EasyChair Preprint 15051, 2024.

Kordzanganeh, M., Sekatski, P., Fedichkin, L., and Melnikov, A. An exponentially-growing family of universal quantum circuits. *Machine Learning: Science and Technology*, 4(3):035036, August 2023. ISSN 2632-2153. doi: 10.1088/2632-2153/ace757. URL <http://dx.doi.org/10.1088/2632-2153/ace757>.

Larocca, M., Thanasilp, S., Wang, S., Sharma, K., Bi-amonte, J., Coles, P. J., Cincio, L., McClean, J. R., Holmes, Z., and Cerezo, M. A review of barren plateaus in variational quantum computing, 2024. URL <https://arxiv.org/abs/2405.00781>.

Mitarai, K., Negoro, M., Kitagawa, M., and Fujii, K. Quantum circuit learning. *Physical Review A*, 98(3), September 2018. ISSN 2469-9934. doi: 10.1103/physreva.98.032309. URL <http://dx.doi.org/10.1103/PhysRevA.98.032309>.

- Niazi, S. K. Quantum mechanics in drug discovery: A comprehensive review of methods, applications, and future directions. *International Journal of Molecular Sciences*, 26(13), 2025. ISSN 1422-0067. doi: 10.3390/ijms26136325. URL <https://www.mdpi.com/1422-0067/26/13/6325>.
- Pedregosa, F., Varoquaux, G., Gramfort, A., Michel, V., Thirion, B., Grisel, O., Blondel, M., Prettenhofer, P., Weiss, R., Dubourg, V., et al. Scikit-learn: Machine learning in python. *Journal of machine learning research*, 12(Oct):2825–2830, 2011.
- Pérez-Salinas, A., López-Núñez, D., García-Sáez, A., Forn-Díaz, P., and Latorre, J. I. One qubit as a universal approximant. *Phys. Rev. A*, 104:012405, Jul 2021. doi: 10.1103/PhysRevA.104.012405. URL <https://link.aps.org/doi/10.1103/PhysRevA.104.012405>.
- Peters, E. and Schuld, M. Generalization despite overfitting in quantum machine learning models. *Quantum*, 7:1210, December 2023. ISSN 2521-327X. doi: 10.22331/q-2023-12-20-1210. URL <http://dx.doi.org/10.22331/q-2023-12-20-1210>.
- Pérez-Salinas, A., Rad, M. Y., Barthe, A., and Dunjko, V. Universal approximation of continuous functions with minimal quantum circuits, 2025. URL <https://arxiv.org/abs/2411.19152>.
- Ragone, M., Bakalov, B. N., Sauvage, F., Kemper, A. F., Ortiz Marrero, C., Larocca, M., and Cerezo, M. A lie algebraic theory of barren plateaus for deep parameterized quantum circuits. *Nature Communications*, 15 (1), August 2024. ISSN 2041-1723. doi: 10.1038/s41467-024-49909-3. URL <http://dx.doi.org/10.1038/s41467-024-49909-3>.
- Schuld, M., Sweke, R., and Meyer, J. J. Effect of data encoding on the expressive power of variational quantum-machine-learning models. *Physical Review A*, 103(3), March 2021. ISSN 2469-9934. doi: 10.1103/physreva.103.032430. URL <http://dx.doi.org/10.1103/PhysRevA.103.032430>.
- Shin, S., Teo, Y. S., and Jeong, H. Exponential data encoding for quantum supervised learning. *Physical Review A*, 107(1), January 2023. ISSN 2469-9934. doi: 10.1103/physreva.107.012422. URL <http://dx.doi.org/10.1103/PhysRevA.107.012422>.
- Turán, P. Sur les fonctions bornées et intégrables. In Turán, P. (ed.), *Leopold Fejér Gesammelte Arbeiten I*, pp. 37–43. Birkhäuser, Basel, 1970.
- Wierichs, D., Kottmann, K., and Killoran, N. Unitary synthesis with optimal brick wall circuits, 2025. URL <https://arxiv.org/abs/2511.16736>.
- Yu, Z., Yao, H., Li, M., and Wang, X. Power and limitations of single-qubit native quantum neural networks. In *Advances in Neural Information Processing Systems*, volume 35, pp. 2751–2764, 2022. URL https://proceedings.neurips.cc/paper_files/paper/2022/file/b250de41980b58d34d6aad3f4aedd4c-Paper-Conference.pdf.
- Yu, Z., Chen, Q., Jiao, Y., Li, Y., Lu, X., Wang, X., and Yang, J. Z. Non-asymptotic approximation error bounds of parameterized quantum circuits, 2024. URL <https://arxiv.org/abs/2310.07528>.

A. Improved Encoding Gate Complexity with Ternary Encoding

This appendix provides the detailed proof supporting the parameter scaling analysis in Section 3. We extend Corollary 2 from Pérez-Salinas et al. (2025) by demonstrating that ternary encoding as described in Shin et al. (2023); Peters & Schuld (2023) creates a dense frequency spectrum with only $k = \mathcal{O}(\log_3 w)$ encoding gates.

Following Pérez-Salinas et al. (2025), we use the normalized domain $x \in [0, 1]$ for the theoretical analysis. This result generalizes straightforwardly to any compact interval through appropriate rescaling of the input variable. In practice, data normalization to intervals such as $[-\pi, \pi]$ is common and also used in our experiments. Throughout the theoretical analysis, we adopt Fourier bases of the form $e^{in\pi x}$ for mathematical convenience; this corresponds to a rescaling of the input and is without loss of generality. We also use the notation w to denote maximum frequency throughout this appendix, which corresponds to ω_{\max} in the main text. We adopt this notation to maintain consistency with the cited proof.

Before presenting the main result in Section A.3, we provide the necessary mathematical components.

A.1. Circuit Architecture

Definition A.1 (Ternary Encoding Circuit with WSW Architecture). A ternary encoding quantum circuit with k encoding gates follows the WSW (Weight-Signal-Weight) architecture introduced in Section 2:

$$U_k^{\text{ternary}}(\boldsymbol{\theta}, x) = W_k(\boldsymbol{\theta}_k) \cdot S_{k-1}(x) \cdot W_{k-1}(\boldsymbol{\theta}_{k-1}) \cdots S_1(x) \cdot W_1(\boldsymbol{\theta}_1) \cdot S_0(x) \cdot W_0(\boldsymbol{\theta}_0), \quad (12)$$

where:

- $S_j(x) = e^{i \cdot 3^j \pi x \sigma_z}$ are fixed encoding gates at exponentially-spaced frequencies $\{3^0, 3^1, 3^2, \dots, 3^{k-1}\}$ (in the π -Fourier basis),
- $W_j(\boldsymbol{\theta}_j)$ are parameterized ansatz blocks with parameters $\boldsymbol{\theta}_j$,
- $x \in [0, 1]$ is the input data,
- $\boldsymbol{\theta} = (\boldsymbol{\theta}_0, \boldsymbol{\theta}_1, \dots, \boldsymbol{\theta}_k)$ denotes all variational parameters.

The parameterized ansatz blocks must provide sufficient expressivity to control all accessible frequencies, as discussed in Theorem A.6.

As established in Section 3, ternary encoding with k gates provides access to all integer frequencies in the range $\Omega_k = \{n \in \mathbb{Z} : |n| \leq M\}$ with $M = (3^k - 1)/2 \approx 3^k/2$ (Shin et al., 2023; Peters & Schuld, 2023). This dense integer coverage is the key property enabling logarithmic scaling in encoding gate count.

By the generalized quantum signal processing framework (Pérez-Salinas et al., 2025), this circuit can be written as:

$$U_k^{\text{ternary}}(\boldsymbol{\theta}, x) = R_M(\boldsymbol{\theta}, x), \quad (13)$$

where R_M is a 2×2 unitary matrix of the form:

$$R_M(\boldsymbol{\theta}, x) = \begin{pmatrix} P_M(x) & -Q_M^*(x) \\ Q_M(x) & P_M^*(x) \end{pmatrix}, \quad (14)$$

with $|P_M(x)|^2 + |Q_M(x)|^2 = 1$ (unitarity condition).

A.2. Mathematical Background

The Frobenius norm is a matrix norm defined as:

$$\|A\|_F = \sqrt{\text{Tr}(A^\dagger A)}. \quad (15)$$

Theorem A.2 (Fejér's Theorem (Turán, 1970)). *Let $f \in C([0, 2])$ be a continuous 2-periodic function, and let*

$$S_N(f)(x) = \sum_{n=-N}^N \hat{f}_n e^{in\pi x}$$

denote the N th partial sum of its Fourier series. Then the Cesàro means

$$\sigma_N(f)(x) = \frac{1}{N+1} \sum_{k=0}^N S_k(f)(x)$$

converge uniformly to f on $[0, 2]$, i.e.,

$$\lim_{N \rightarrow \infty} \sup_{x \in [0, 2]} |\sigma_N(f)(x) - f(x)| = 0.$$

By Theorem 5 in Pérez-Salinas et al. (2025), it is possible to construct arbitrary polynomials $P(e^{ix})$ of degree at most M such that the matrix R_M in Equation (14) approximates the target encoding:

$$R_M(\boldsymbol{\theta}, x) \approx \begin{pmatrix} e^{iwx} & 0 \\ 0 & e^{-iwx} \end{pmatrix} = e^{iwx\sigma_z}, \quad (16)$$

where w is the target frequency. The key insight is that $P_M(x)$ can be chosen as a Cesàro mean of the function e^{iwx} , which converges uniformly by Fejér's theorem.

Definition A.3 (Cesàro Means). Let $f : \mathbb{R} \rightarrow \mathbb{C}$ be a continuous function with period 2π , and let $S_n(x) = \sum_{j=-n}^n c_j e^{ij\pi x}$ be its n -th partial Fourier sum. The Cesàro mean of order M is given by

$$P_M(x) = \frac{1}{M+1} \sum_{n=0}^M S_n(x) = \sum_{n=-M}^M \frac{M+1-|n|}{M+1} c_n e^{in\pi x}, \quad (17)$$

where c_n are the Fourier coefficients of f . The equality holds by counting: each coefficient c_n appears in $(M+1-|n|)$ partial sums.

With this choice of $P_M(x)$, the Frobenius norm of the approximation error can be expressed as:

$$\|R_M(\boldsymbol{\theta}, x) - e^{iwx\sigma_z}\|_F = \sqrt{2} \sqrt{|P_M(x) - e^{iwx}|^2 + |Q_M(x)|^2}. \quad (18)$$

Using the reverse triangle inequality and the unitarity condition $|P_M|^2 + |Q_M|^2 = 1$, we can derive a useful bound. Since $|e^{iwx}| = 1$, we have:

$$|e^{iwx} - P_M(x)| \geq 1 - |P_M(x)| \geq \frac{1 - |P_M(x)|^2}{2} = \frac{|Q_M(x)|^2}{2}, \quad (19)$$

therefore the Frobenius norm can be bounded as:

$$\|R_M(\boldsymbol{\theta}, x) - e^{iwx\sigma_z}\|_F \leq \sqrt{2} \sqrt{|e^{iwx} - P_M(x)|^2 + 2|e^{iwx} - P_M(x)|}. \quad (20)$$

With Fejér's theorem (Theorem A.2), the supremum of this norm can be made arbitrarily small provided e^{iwx} satisfies the continuity and periodicity requirements. This is ensured by using an auxiliary function that extends e^{iwx} periodically:

$$a(x) = \begin{cases} e^{iwx}, & \text{if } 0 \leq x \leq 1, \\ e^{iw(2-x)}, & \text{if } 1 < x < 2. \end{cases} \quad (21)$$

This function is continuous, periodic with period 2, and equals e^{iwx} on $[0, 1]$. Since the ternary encoding circuit can express polynomials of $e^{in\pi x}$ for all $n \in \Omega_k$, we can construct the Cesàro mean of $a(x)$, ensuring

$$\sup_{x \in [0, 1]} \|R_M(\boldsymbol{\theta}, x) - e^{iwx\sigma_z}\|_F \leq \epsilon. \quad (22)$$

A.3. Main Result: Encoding Gate Complexity

We now present the complete proof of Corollary 5.3, which appears in simplified form in Section 5. This detailed version extends Corollary 2 from Pérez-Salinas et al. (2025) and demonstrates the exponential improvement achievable through ternary encoding.

Corollary A.4 (Ternary Encoding Gate Complexity - Detailed Version). *The ternary encoding circuit $U_k^{\text{ternary}}(\theta, x)$ from Equation (13) can approximate $e^{iwx\sigma_z}$ to precision ϵ using*

$$k \in \mathcal{O}\left(\log_3 w + \log_3\left(\frac{1}{\epsilon}\right)\right) \quad (23)$$

fixed encoding gates $\{S_j(x) = e^{i \cdot 3^j \pi x \sigma_z}\}_{j=0}^{k-1}$, where we suppress doubly-logarithmic correction factors such as $\log \log(1/\epsilon)$ arising from harmonic series bounds. This represents an exponential improvement over unary encoding, which requires $N \in \tilde{\mathcal{O}}(w + \epsilon^{-2})$ encoding gates.

Proof. The proof proceeds by showing that ternary encoding enables efficient approximation for both the coarse frequency component (large w) and fine precision requirements (small ϵ).

Ternary Encoding Density. By Shin et al. (2023); Peters & Schuld (2023), ternary encoding with k gates at frequencies $\{3^0, 3^1, \dots, 3^{k-1}\}$ provides access to all integer frequencies in $\Omega_k = \{n \in \mathbb{Z} : |n| \leq M\}$ where $M = (3^k - 1)/2 \approx 3^k/2$. This is the key enabling property: k ternary gates provide access to $M \approx 3^k/2$ distinct integer frequencies.

Coarse Frequency Approximation. Any target frequency $w \in \mathbb{R}$ can be decomposed as $w = K\pi + w'$ where K is an integer and $|w'| \leq \pi/2$. The integer component K determines the required frequency range that must be accessible in the spectrum. For ternary encoding to cover this range:

$$M \geq K \quad \Rightarrow \quad \frac{3^k - 1}{2} \geq \frac{w}{\pi} \quad \Rightarrow \quad k \geq \log_3\left(\frac{2w}{\pi} + 1\right) = \mathcal{O}(\log_3 w). \quad (24)$$

This establishes the logarithmic dependence on the target frequency magnitude.

Fine Precision Approximation. The auxiliary function $a(x)$ from Equation (21) has Fourier coefficients

$$c_n = -i \frac{w \left((-1)^n e^{iw} - 1\right)}{w^2 - (n\pi)^2}. \quad (25)$$

Since Ω_k contains all integers in $[-M, M]$, we construct the Cesàro mean:

$$P_M(x) = \sum_{n=-M}^M \frac{M+1-|n|}{M+1} c_n e^{in\pi x}. \quad (26)$$

The approximation error decomposes into two terms representing truncation within and beyond the accessible frequency range:

$$P_M(x) - e^{iwx} = \sum_{n=-M}^M c_n \frac{-|n|}{M+1} e^{in\pi x} - \sum_{|n|=M+1}^{\infty} c_n e^{in\pi x}. \quad (27)$$

Applying the triangle inequality and taking the supremum over $x \in [0, 1]$:

$$\sup_{x \in [0, 1]} |P_M(x) - e^{iwx}| \leq \frac{2}{M+1} \left| \sum_{n=1}^M n c_n \right| + 2 \left| \sum_{n=M+1}^{\infty} c_n \right|. \quad (28)$$

For the fractional component with $|w'| \leq \pi/2$, the first term in Equation (28) is bounded by:

$$\left| \sum_{n=1}^M n c_n \right| \leq \sum_{n=1}^M n |c_n| \leq \frac{2}{\pi} \sum_{n=1}^M \frac{n}{n^2 - 1/4} \quad (29)$$

$$\leq \frac{2}{\pi} \left(\frac{4}{3} + \int_1^M \frac{x dx}{x^2 - 1/4} \right) = \frac{2}{\pi} \left(\frac{4}{3} + \frac{1}{2} \log \left(\frac{4M^2 - 1}{3} \right) \right). \quad (30)$$

The second term (tail sum beyond the accessible range) is bounded by:

$$\left| \sum_{n=M+1}^{\infty} c_n \right| \leq \frac{2}{\pi} \int_M^{\infty} \frac{dx}{x^2 - 1/4} \leq \frac{2}{\pi} \frac{1}{M - 1/4}. \quad (31)$$

Since the first term dominates asymptotically, we obtain:

$$\sup_{x \in [0,1]} |P_M(x) - e^{iwx}| \in \mathcal{O}(M^{-1} \log M) = \mathcal{O}(k \cdot 3^{-k}), \quad (32)$$

where we used $M \approx 3^k/2$ which implies $\log M \approx k \log 3$. For complexity analysis, we absorb the logarithmic factor, giving $\mathcal{O}(3^{-k})$.

Matrix Error via Frobenius Norm. From Equation (18) and the unitarity bounds derived above:

$$\|R_M(\boldsymbol{\theta}, x) - e^{iwx\sigma_z}\|_F \leq \sqrt{2} \sqrt{|P_M(x) - e^{iwx}|^2 + 2|P_M(x) - e^{iwx}|}. \quad (33)$$

For small errors where $|P_M(x) - e^{iwx}| \leq 1$, we have $|P_M(x) - e^{iwx}|^2 \leq |P_M(x) - e^{iwx}|$, yielding:

$$\|R_M(\boldsymbol{\theta}, x) - e^{iwx\sigma_z}\|_F \leq \sqrt{6|P_M(x) - e^{iwx}|}. \quad (34)$$

Therefore, combining with the pointwise error bound:

$$\sup_{x \in [0,1]} \|R_M(\boldsymbol{\theta}, x) - e^{iwx\sigma_z}\|_F \in \mathcal{O}(M^{-1/2} \sqrt{\log M}) = \mathcal{O}(\sqrt{k} \cdot 3^{-k/2}). \quad (35)$$

Precision Requirement. To achieve precision ϵ , we require:

$$C\sqrt{k} \cdot 3^{-k/2} \leq \epsilon, \quad (36)$$

$$3^{k/2} \geq \frac{C\sqrt{k}}{\epsilon}, \quad (37)$$

$$\frac{k}{2} \geq \log_3 \left(\frac{C}{\epsilon} \right) + \frac{1}{2} \log_3 k. \quad (38)$$

Solving yields $k = \mathcal{O}(\log_3(1/\epsilon) + \log \log(1/\epsilon))$. Since the doubly-logarithmic term is negligible:

$$k \in \mathcal{O}(\log_3(1/\epsilon)), \quad (39)$$

where $C = \mathcal{O}(\sqrt{w})$ absorbs the dependence on the target frequency.

Total Encoding Gate Complexity. Combining the requirements from coarse frequency coverage and fine precision:

$$k \geq \max \{ \mathcal{O}(\log_3 w), \mathcal{O}(\log_3(1/\epsilon)) \} = \mathcal{O}(\log_3 w + \log_3(1/\epsilon)), \quad (40)$$

giving the number of fixed encoding gates required. □

Remark A.5 (Comparison with Unary Encoding). Corollary 2 in Pérez-Salinas et al. (2025) establishes that unary encoding requires $N \in \tilde{\mathcal{O}}(w + \epsilon^{-2})$ fixed encoding gates, where the $\tilde{\mathcal{O}}$ notation hides logarithmic factors. In contrast, ternary encoding requires only $k \in \mathcal{O}(\log_3 w + \log_3(1/\epsilon))$ encoding gates, representing an exponential improvement in both the frequency dependence ($w \rightarrow \log_3 w$) and precision dependence ($\epsilon^{-2} \rightarrow \log_3(1/\epsilon)$).

Remark A.6 (Parameter Requirements and Total Complexity). While Theorem A.4 establishes that only $k \in \mathcal{O}(\log_3 w + \log_3(1/\epsilon))$ fixed encoding gates are required, the parameterized ansatz blocks $\{W_j(\boldsymbol{\theta}_j)\}$ must have sufficient expressivity to represent arbitrary functions over the accessible frequency range Ω_k .

By fundamental expressivity results (Schuld et al., 2021), representing arbitrary functions with integer-valued frequency spectrum $[-M, M]$ requires at least $2M + 1$ independent parameters. Since $M \approx 3^k/2$, the total number of variational parameters scales as:

$$|\boldsymbol{\theta}| = \mathcal{O}(M) = \mathcal{O}(3^k) = \mathcal{O}(w). \quad (41)$$

The total gate count consists of: (1) $k = \mathcal{O}(\log_3 w)$ encoding gates, and (2) $|\boldsymbol{\theta}| = \mathcal{O}(w)$ parameter gates in the ansatz blocks. Therefore, while ternary encoding reduces the number of encoding gates exponentially compared to unary encoding ($\mathcal{O}(\log w)$ versus $\mathcal{O}(w)$), both approaches require $\mathcal{O}(w)$ total gates when parameter gates are included. The total circuit complexity is dominated by the parameter requirements in both cases, resulting in **linear scaling** in the maximum frequency w (or equivalently, M or Λ as used in different sections).

B. Experimental Results for Identical Unary Prefactor Starting Values

As mentioned in Section 4, the optimizer faced difficulties in updating all 3 prefactor values simultaneously when identical initial values of $\{1.0, 1.0, 1.0\}$ were chosen. Figure 5 shows that only with a learning rate (lr) of 0.1 did the prefactors evolve to 3 different values. For smaller learning rates of 0.001 and 0.01, two of the three prefactors remained identical throughout the optimization, as they received identical gradient signals. Comparing the achieved R^2 scores for the different starting values in Figure 6 reveals, however, that there was no significant difference in the fitting quality between identical initialization $\{1.0, 1.0, 1.0\}$ and perturbed initialization $\{1.01, 1.02, 1.03\}$.

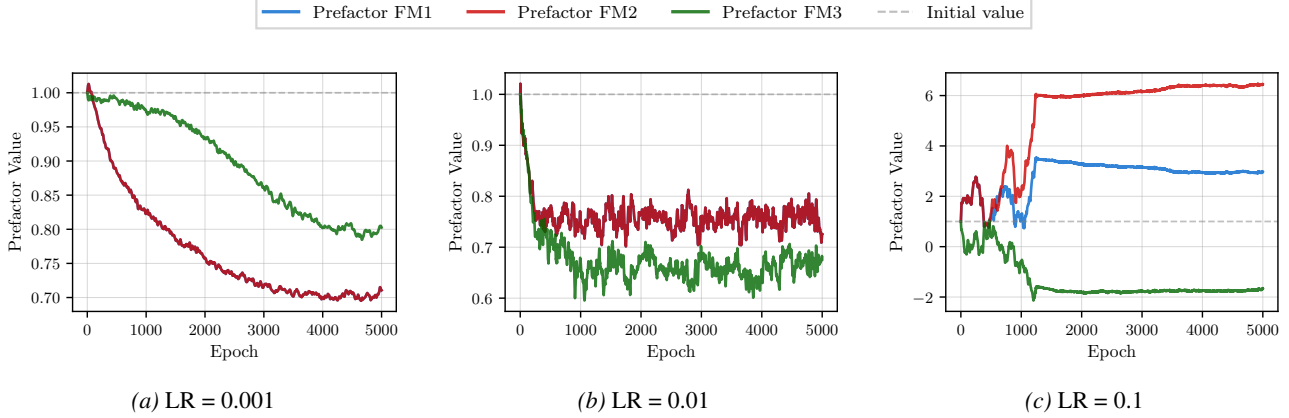
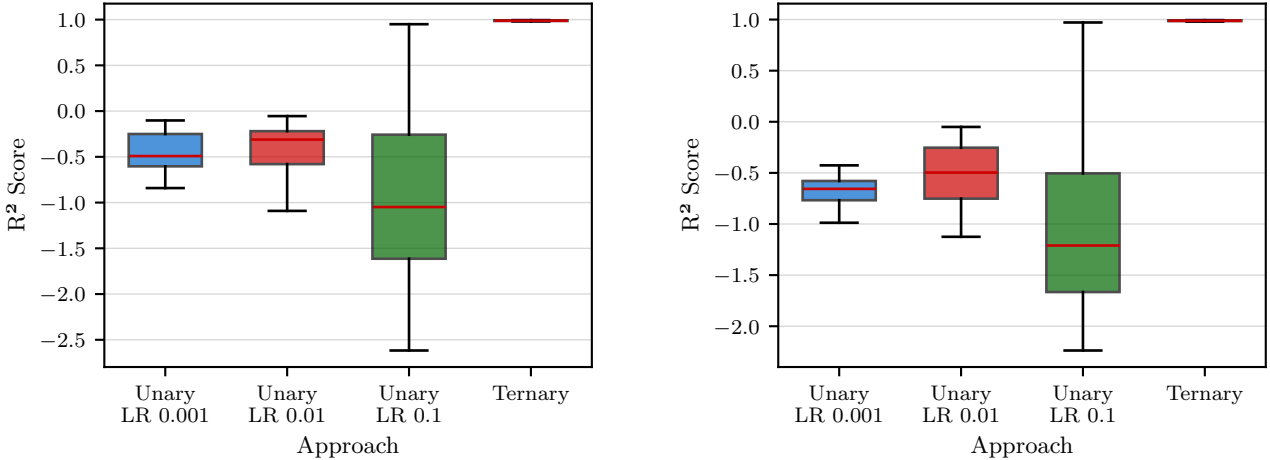


Figure 5. Prefactor evolution for different learning rates with initial prefactors of $\{1.0, 1.0, 1.0\}$. For each learning rate, the evolution shows the prefactors during training for the experiment with the highest R^2 score. With learning rates of 0.001 and 0.01, prefactors remain coupled and evolve identically.



(a) R^2 scores with identical unary initial prefactors $\{1.0, 1.0, 1.0\}$ (learning rates 0.001, 0.01, 0.1) versus trainable ternary prefactors (lr 0.001).

(b) R^2 scores with perturbed initial prefactors $\{1.01, 1.02, 1.03\}$ (learning rates 0.001, 0.01, 0.1) versus trainable ternary prefactors (lr 0.001).

Figure 6. R^2 score distributions for 100 target functions with frequency spectrum $\Omega_2 = \{11, 11.2, 13\}$ across all learning rates, comparing identical (a) and perturbed (b) unary prefactor initializations. Despite different prefactor evolution patterns, both initialization strategies yield similar performance distributions.

C. Real World Dataset Results

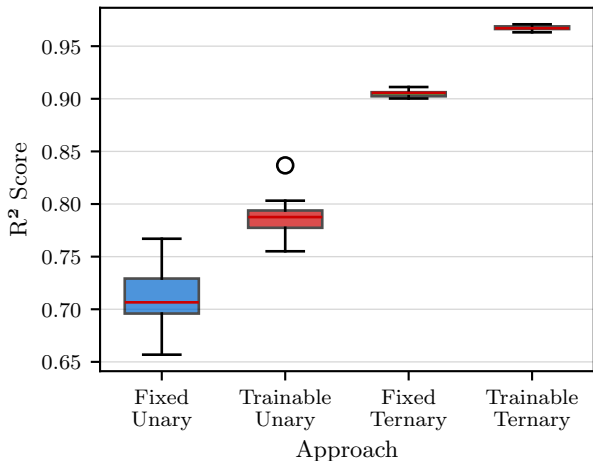


Figure 7. R^2 scores for 10 random initializations for the Flight Passengers dataset.

D. Experimental Setup Details

We use evenly spaced points across $[-\pi, \pi]$ with 100 sample points. To ensure compatibility with quantum rotational gate requirements, we apply Scikit-Learn’s MinMaxScaler (Pedregosa et al., 2011) to scale target outputs to $[-1, 1]$.

Our experimental implementation utilizes PennyLane (version 0.42.0) (Bergholm et al., 2022) with JAX/JIT compilation (version 0.5.0) (Frostig et al., 2018) for enhanced computational performance. All training and inference operations were executed on a MacBook Pro equipped with an Apple M2 processor, 16 GB memory, and running macOS Sequoia 15.5.

We employ DeepMind’s Optax Adam optimizer (DeepMind, 2020) with a fixed learning rate of 0.001 for 5000 training iterations. Model validation follows an 80/20 train-test split protocol. To demonstrate the effectiveness of our frequency selection techniques, we deliberately use these standard hyperparameters without further optimization, showing that our approaches achieve expected target function fitting performance where conventional models fail under identical conditions.

All ansatz parameters are initialized with a value of 1 as in Jaderberg et al. (2024). Mean squared error serves as the optimization objective, while R^2 scores provide the primary performance evaluation metric. Results are summarized using interquartile ranges (IQRs), with error bars representing the spread between the 25th and 75th percentiles around the mean R^2 score.

E. Circuit Diagram

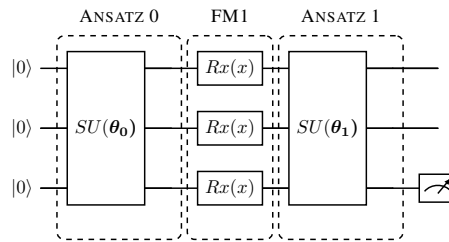


Figure 8. 3-qubit circuit architecture with 3-qubit Special Unitary (SU) gates used in the experimental validation. The circuit employs one feature map layer with parallel encoding across all qubits, interleaved with ansatz blocks providing 63 trainable parameters per layer.